IOP Publishing Measurement Science and Technology
Meas. Sci. Technol. **31** (2020) 055403 (18pp) https://doi.org/10.1088/1361-6501/ab614f

Depth-of-field reduction due to blurring in a relayed plenoptic camera and mitigation via deconvolution

Zu Puayen Tan and Brian S Thurow

Aerospace Engineering, Auburn University, Auburn, AL, United States of America

E-mail: zzt0012@auburn.edu

Received 24 October 2019, revised 9 December 2019
Accepted for publication 12 December 2019
Published 31 January 2020

Abstract

The projection of an externally-mounted microlens array (MLA) onto a sensor via relay lenses is oft adopted by the scientific community in lieu of traditional plenoptic cameras with embedded on-sensor MLAs. In most cases a relayed design better supports prototyping and temporary setups, while in other cases such as intensified plenoptic imaging the extended projection distance is necessary due to physical constraints. However, relaying the MLA inevitably blurs the raw image, often by 1.5 px or more. We observed an unusual behavior where fixed blurring at the raw image level produced blurs that are worsened by depth within refocused images – enough to reduce the plenoptic system's depth-of-field by 60% in most cases. To address this problem, we hereby put forth a model to elucidate the mechanism of this depth-dependent blurring, and propose a Lucy–Richardson deconvolution procedure for mitigation. Discussions are undertaken in the contexts of regular and intensified plenoptic photography, as well as application in 3D particle image velocimetry for fluid dynamics. Results were validated on synthetic as well as experimental images.

Keywords: light-field, plenoptic, optical relay, 3D particle image velocimetry, tomographic reconstruction, point-spread-function, Lucy–Richardson deconvolution

(Some figures may appear in colour only in the online journal)

1. Introduction

The plenoptic camera was originally developed by Adelson and Wang [1], Levoy [2], Lumsdaine and Georgiev [3], Wu *et al* [4] and Ng *et al* [5] for post-capture refocusing and range-finding. However, owing to increasingly powerful camera sensors and computational tools in recent years, plenoptic cameras have enjoyed growing popularity in an expanding range of applications [6], with notable examples including photography [5], occlusion-detection/depth-estimation [7] and machine-vision [8, 9]. Similarly, the experimental fluid dynamics community, including our group, has adopted the plenoptic camera for monocular 3D flow-measurements [10–17], which represents a lower-cost, simpler-configuration alternative to traditional approaches where four or more cameras are required.

These powerful applications of the plenoptic camera are enabled by the unique manner the camera samples a light-field. As illustrated in figure 1 and described in [5], a scene's four-dimensional (4D) light-field with spatial dimensions s,t and angular dimensions u,v is captured by a plenoptic camera's monocular main lens, followed by passage through a dense microlens array (MLA) located at the main lens' image plane. Each microlens projects the incident rays onto the sensor as a small circular 'sub-image'. The position of a sub-image corresponds to the incident ray's s,t coordinate while pixel position within each sub-image corresponds to the incident ray angle (u,v) for a given s,t.

In post-processing, a unique *perspective view* can be generated by sampling the same (u,v) pixel behind every microlens and assembling them into an image. On the other hand, a *refocused image* with fixed perspective can be generated by

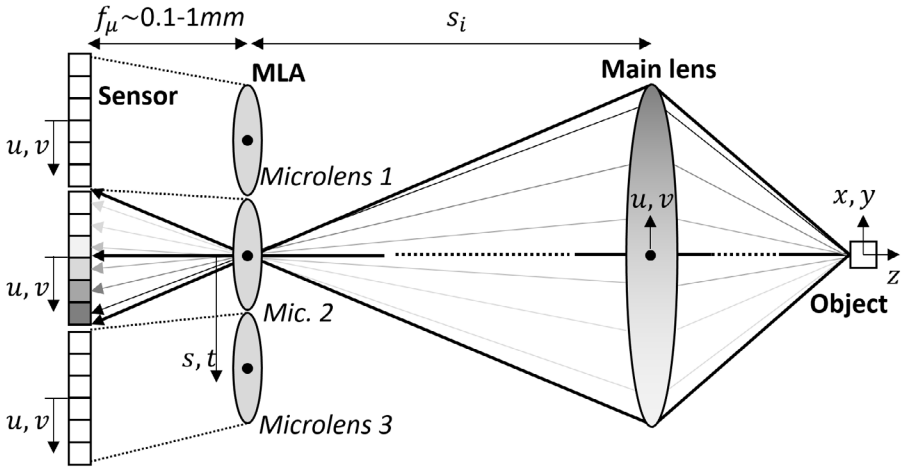

Figure 1. Principles of plenoptic imaging.

projecting rays from the sensor plane outwards to a virtual image plane, after which all rays falling within each sub-image are averaged to form one refocused image's pixel. Notably, a subject's 3D location (x,y,z) in object space can be determined by tracking it across multiple perspective view and applying the principles of parallax.

Though plenoptic cameras have many applications, its utility in 3D flow-measurements is the basis of our motivation and many of this paper's analyses. In a common 3D flow-measurement application called plenoptic particle image velocimetry (PPIV) [10–12], a volume of fluid is seeded with flow-tracing particles that are illuminated by a pulsed light source. The volume is imaged by one or two plenoptic cameras. The set of all possible perspective views is then generated and used to reconstruct the original 3D particle field using tomographic techniques such as the algebraic reconstruction technique (ART):

$$E(x,y,z)^{k+1} = E(x,y,z)^{k} + \mu \frac{I(s,t) - \sum_{xyz} w_{xyz,st} E(x,y,z)^{k}}{\sum_{xyz} w_{xyz,st}^{2}} \tag{1}$$

or multiplicative algebraic reconstruction technique (MART):

$$E(x,y,z)^{k+1} = E(x,y,z)^{k} \left[\frac{I(s,t)}{\sum_{xyz} w_{xyz,st} E(x,y,z)^{k}} \right]^{\mu w_{xyz,st}} \tag{2}$$

where E is the volume's voxel intensity at position (x, y, z) on the kth iteration. I is the perspective view's pixel intensity at location (s, t), w is the weighting function that relates E to I, and μ is a relaxation parameter. Cross-correlation or particle tracking can then be performed on two sequentially-captured particle fields to determine the instantaneous 3D velocity-field. With similar approaches, 3D fields of scalar values (e.g. a 3D fluid density field [13] or 3D flame [14, 15]) can also be measured by plenoptic cameras.

PPIV has proved to be an attractive low-cost, small footprint (albeit also lower resolution) alternative to the standard practice of multi-camera 3D flow-measurements, which typically employs four cameras for PIV and five or more for scalar-fields. Another particularly attractive feature of the plenoptic camera, when compared against multi-camera systems, is the extended depth-of-field (DOF) it can achieve due to the camera's refocusing capability, which directly results in the ability to measure deeper volumes for a given illumination intensity.

Despite numerous advantages, a plenoptic camera is inherently difficult to design because the plenoptic-enabling MLA must be installed within one microlens focal length (f_μ ~ 0.1–2 mm) of the camera sensor in a Plenoptic 1.0 architecture. This constraint limits implementation to purpose-made or heavily modified cameras. For example, our early works on PPIV relied on Imperx Bobcat B4820/B66x0 cameras that had their sensor-protection glass removed and internal structures carved out to accommodate the MLA [10–13]. This constraint is increasingly untenable in our efforts to expand plenoptic capabilities to kHz-rate high-speed imaging for time-resolved measurements and to intensifiers for UV/IR and night-vision imaging. Particularly, (i) the risks and costs of modifying a high-speed camera is unacceptable, (ii) logistically, as a high-cost shared resource, the high-speed camera/intensifier must be easily convertible between plenoptic and regular-imaging, and (iii) the thick ~5 mm intensifier entrance window separating MLA from photocathode cannot satisfy the one focal length constraint.

Thus, as described in [16, 17] and shown in figure 2, we recently adopted a relayed plenoptic architecture for the development of high-speed/intensified plenoptic systems at our lab. This architecture relocates the MLA to an external housing and the MLA image-plane (traditionally coincident with the sensor) is now optically relayed onto a sensor far downstream. The *physical* one focal length constraint is thereby relaxed, and conversion of off-the-shelf cameras/intensifiers to plenoptic-imaging becomes easily achievable through attaching the relay lens and MLA via standard lens mount.

Historically, the relayed architecture was first used by Adelson and Wang [1] in their pioneering plenoptic work, while subsequent adoptions include: Dansereau *et al* [9] who designed a monocentric-lens wide field-of-view plenoptic camera, Drazic *et al* [18] who designed a plenoptic video-streaming camera, Levoy *et al* [19, 20] for plenoptic microscopy, Liu *et al* [21] for flame-imaging and Fischer *et al*'s [22] for multi-plane particles Doppler velocimetry. Most of these works implemented the relayed architecture for flexibility.

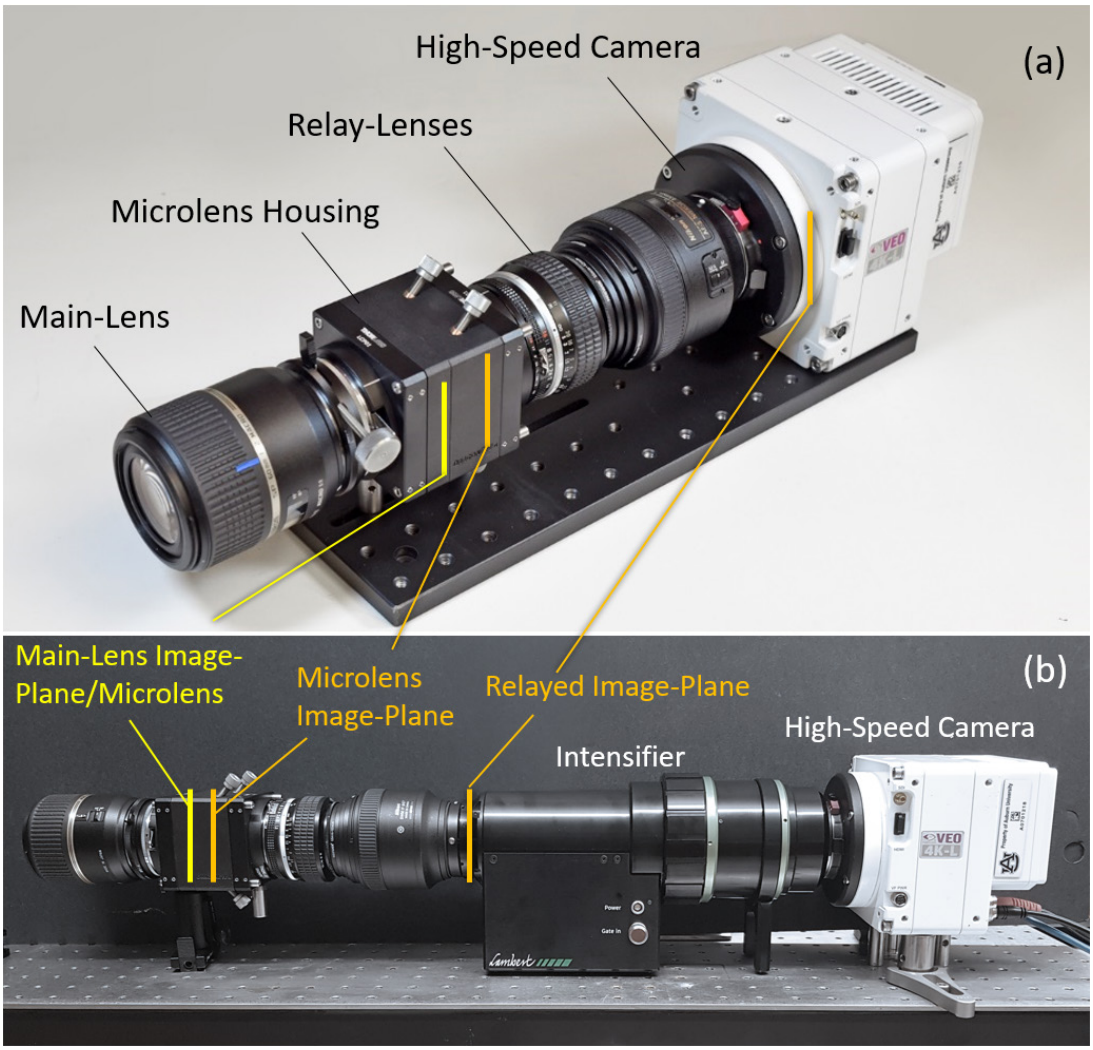

Figure 2. (a) The high-speed relayed-plenoptic camera system with (b) its intensified counterpart.

With the advantage of flexibility comes the downside of inevitable blurring introduced by the relay lens *between* the MLA and sensor. In regular 2D imaging, lens blur merely results in softening of the image by a degree proportional to the lens' point spread function (PSF). However, in a plenoptic camera, we observed a peculiar behavior where blurring of the relayed image produced softening that *increased* the further an image was refocused away from its nominal focal-plane. This resulted in a loss of DOF in refocused images, and the inability to reconstruct 3D objects across the same depth range as comparable embedded-MLA plenoptic cameras. With the discovery of this critical downside to relayed plenoptic, we conducted this study:

i. to quantitatively characterize the impact of relay blur using both synthetic and experimental plenoptic images;
ii. to put forth a theoretical model for the behavior;
iii. finally, to propose a Lucy–Richardson deconvolution (LRD) procedure for mitigating blurring's impact.

Although primarily motivated by PPIV and intensified plenoptic imaging, the presented results apply to general relayed plenoptic systems. The paper is organized in terms of methodology of study, analyses based on synthetic images, proposition of a theoretical model, attempt at mitigation via LRD and finally validation via experimental data.

2. Methodology

Tests were designed to elucidate the impact of blurring on (i) refocused images and (ii) 3D reconstruction of particle-fields for PPIV application. The tests made use of synthetically generated plenoptic images to exclude tertiary effects such as camera noise, as well as experimental images for validation.

Blurring's impact on *refocusing* was quantified using images of dots with known dimensions and locations. In the case of synthetic images, this consists of a grid of point light sources at various specified distances from the camera. For experimental images, this consists of a flat metal plate with gridded dots that was precisely translated parallel to the camera's optical axis. Both non-intensified and intensified plenoptic cameras were used for experiment. Different degrees of blurring were either synthetically simulated or experimentally applied, and their effects on the ability to refocus the point source/dots were characterized.

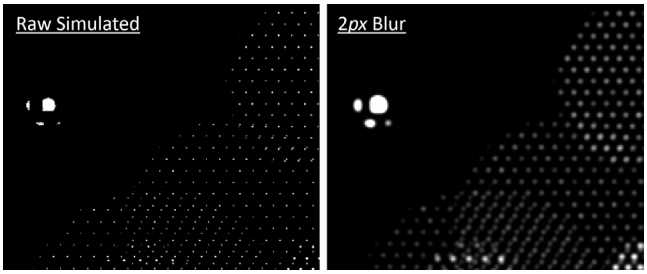

Figure 3. Zoomed-in raw and blurred synthetic particle image.

On the other hand, the impact of blurring on *3D reconstruction* was assessed based on synthetic and experimental images of particle-filled volumes, which resemble scenes found in PPIV applications. Different degrees of blur were once again applied, and MART was performed on the subsequent images to reconstruct the 3D particle fields. In the case of synthetic images, the true particle locations were known. We can thus quantify the impact of blurring on the volume's 3D accuracy along with particle-to-background contrast (i.e. SNR). In the experimental case, only SNR can be characterized.

Finally, benefits gained from sharpening the blurred images via LRD were assessed on all data sets. Details of our image synthesis and acquisition procedures are as follow:

2.1. Synthetic images

The ray-tracing simulator described in [10, 11] was used for image synthesis. The synthetic camera contained a hexagonally-packed MLA with a focal length of $f_\mu = 0.308$ mm and F-number of 4, while the sensor size was $36 \times 24\,\text{mm}^2$ with 6600×4400 px, all of which are identical to our embedded-MLA Imperx plenoptic cameras [10–13].

Synthetic images of the 3D particle fields were generated with particle densities of 0.009–0.045 particles per microlens (i.e. 500–5000 particles), within the low to average range for PPIV. All particles were point sources (i.e. thus characterizing the total system's PSF) and randomly distributed within a volume spanning 48 mm across, 48 mm high and 50 mm deep, captured through a synthetic 85 mm main lens with magnification of $M_{\text{main}} = -0.5$. In contrast, images to assess refocusing sharpness were synthesized with only a sparse grid of points located from $z = -50$ to 50 mm. No overlap exists between points and blurring on each point can be precisely measured.

Different degrees of relay blurring were simulated by Gaussian blurring the images with kernels of $\sigma = 0.5,1,1.5,2$ px – a typical profile and size for our relay system as we will later show. A comparison of the synthetic particle image with its blurred counterpart is given in figure 3. Particles near the nominal focal-plane appear as large spots spanning only a few microlenses (e.g. the group of four spots near the left edge), while particles far from the focal-plane are dimmer, point-like and spread across many microlenses (e.g. the clusters of single-pixel dots on the right). In the blurred case, each dot can be seen to span significantly larger number of pixels.

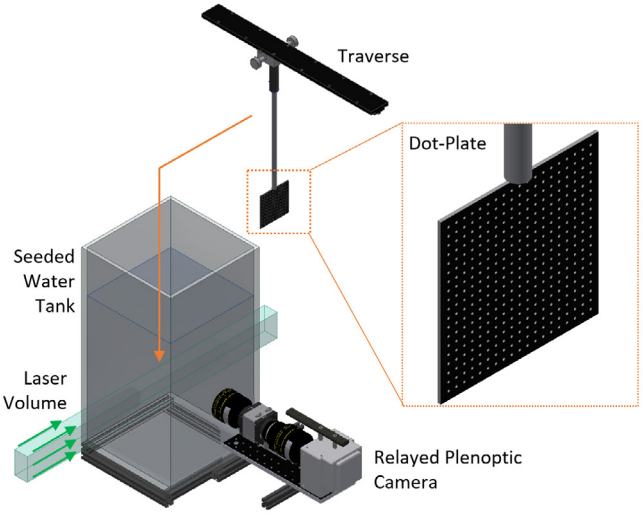

Figure 4. Experimental setup to capture particle-field and dot images.

2.2. Experimental images

Experimental images of particle fields and dot grids were acquired using the setup in figure 4, which consists of a square water tank with a suspension of 10 μm hollow-sphere glass particles. Imaging was performed by the non-intensified relayed plenoptic camera in figure 2. The system was composed of a Vision Research Phantom VEO4k 1 kHz camera with a 27.6×15.5 mm (4096×2160 px) sensor, coupled to a hexagonally-packed MLA with a focal length of $f_\mu = 0.308$ mm and F-number of 4 (identical MLA to the synthetic images). Relay was achieved through a Nikon 50 mm f/1.2 and a Pentax 70 mm f/2.4 lens connected front-to-front and focused at infinity. Notably, this relay produced an added magnification of 1.4, which was necessary to 'zoom' past an otherwise substantial circle of vignette. A refocus image resolution of approximately 256×144 px was achievable assuming 1 px per microlens. Finally, the camera system was completed with a Tamron 60 mm f/2 main lens set at $M_{\text{main}} \approx -0.5$, which resulted in a theoretical maximum DOF of ~40 mm.

To acquire dot-images, a traverse was installed on top of the tank parallel to the optical axis. A flat black metal plate with a grid of white dots 1.5 mm in diameter and spaced 5 mm apart was set perpendicular to the optical axis at the focal-plane. The plate was then translated and imaged across ± 40 mm at 10 mm intervals using fixed camera settings. This z range deliberately exceeded the system's theoretical DOF to characterize performance at extreme depths. Images were first acquired with the camera optimally tuned for sharpness (i.e. baseline condition). One of the relay lenses was then deliberately defocused to simulate blurring encountered in either poor user adjustments or lower-quality relay lenses. In addition to characterizing the camera's refocusing ability, the dot-plate images also serve to generate a 3D calibration for the setup [23], which is necessary to perform 3D reconstruction.

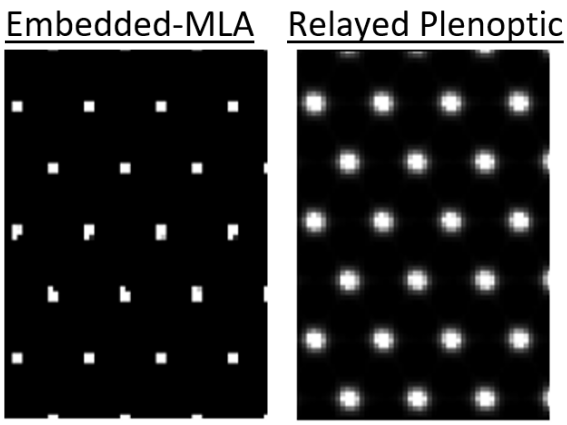

Figure 5. Zoomed-in closed-aperture image.

To acquire particle-field images, the metal plate was removed, the particle-seeded water agitated, and the particles illuminated by a $W = 39\,\text{mm} \times H = 22\,\text{mm} \times D = 45\,\text{mm}$ volume of laser. In post-processing, reconstructions of the 3D particle fields from both experimental and synthetic images were performed using the MART algorithm (see equation (2) and [10–12]). Fifteen iterations of MART with a relaxation of $\mu = 0.2$ was used for the synthetic images, as these parameters were demonstrated to provide smooth, gradual convergence for a plenoptic system [24]. For experimental images, five iterations without relaxation were used to mimic a more realistic procedure where convergence is aggressive and terminated near the first 'overshoot' to conserve computational resources.

Notably, a key distinction between synthetic and experimental images is that MLA position relative to the image is not known *a priori* in the latter case. Determining the relative MLA position involves imaging a flat-white background with the main lens aperture turned down to a minimum (typically *f*/22). Since the MLA is focused on the main lens aperture plane in a 'Plenoptic 1.0' arrangement, the image of the closed aperture appears as a grid of point-like dots (e.g. see figure 5) where each point coincides with the center of a microlens. From figure 5, positions of microlens centers across the entire image can be determined to allow decoding of the 4D light-field data.

The closed-aperture image has a special property that will be exploited in our investigation: on most plenoptic cameras, a closed aperture appears nearly as single-pixel points on the camera sensor. For example, in our arrangement a closed aperture ideally forms a 1.5 px wide dot on the 16 px wide sub-image if blurring is absent. Hence, each dot can be interpreted as an approximation of the PSF for whichever lens element lies between the MLA and sensor (i.e. the relay's PSF). That is, any widening beyond 1.5 px is introduced by blurring through the relay. From figure 5, it is evident that the embedded MLA produced a sharp dot on the order of only 1–2 px across, whereas the relayed system has a Gaussian-like PSF with $\sigma \approx 1.5$ px. This PSF radius provided an approximate value for which to simulate blurring in synthetic images.

2.3. Experimental intensified plenoptic image

Intensified plenoptic imaging was achieved using the system in figure 2. A Lambert Instruments TriCatt 25 intensifier was installed between the relay system and VEO4k camera. The same MLA as previous tests was employed, but the relay was switched to a Nikon 50 mm *f*/1.2 and Nikon 85 mm *f*/1.8 pairing ($M_{\text{relay}} = 1.7$) to expand the size of each sub-image to cater for the intensifier's 69 lp mm^{-1} resolution (i.e. approximate 93% of the camera's sensor resolution). Performance of the system was assessed by imaging the same calibration dot-plate as the particle field experiment. $M_{\text{main-lens}} \approx -0.3$, and the dot-plate was translated across $z = \pm 75\,\text{mm}$ at 25 mm intervals (slightly beyond the system's theoretical maximum DOF of $\pm 50\,\text{mm}$). Imaging was performed outside the water tank. For comparison, a non-intensified version of the system was also employed to image the same target. A non-intensified baseline was captured in an ideal brightly-lit room, while the non-intensified dark-room benchmark was captured when lights were dimmed until subjects were barely resolvable. The intensified system was then employed in the same dark-room condition to assess the effects of intensification.

3. Results and analysis (synthetic image)

3.1. Impacts of relay blurring on refocused images

Figure 6 contains a series of refocused views for a synthetic image that contains 1000 particles. On the left column ('Original'), the raw synthetic image is refocused to the nominal focal-plane ($\alpha = 1$) and two nearside virtual focal planes ($\alpha = 1.05$ and 1.10), where $\alpha \equiv z_i/s_i$ and s_i is the nominal image distance while z_i is the refocus virtual image distance. In contrast, the right column contains the same refocused views *after* the raw image was blurred by a 2 px Gaussian kernel- a realistic degree of relay blur.

We observe from the first row that particles near the nominal focal-plane (blue boxes at $\alpha = 1$) remain sharp despite the 2 px blur. Particles that are out of focus at $\alpha = 1$ (yellow boxes) also appear blurry in both cases. However, when the images were refocused to $\alpha = 1.05$, only the Original case produced sharp particles within the yellow box, whereas the blurred case could not be brought into focus. At $\alpha = 1.10$, the refocus plane is now outside of the particle-containing volume and all particles appear blurred; nonetheless, the circles-of-confusion in the blurred case appear noticeably softer. We thus qualitatively concluded based on figure 6 that the relay blur's impact is exacerbated by refocusing distance.

To quantify the effects of relay blur, a theoretical model is herein proposed based on figure 7. Consider a point source ('True' black circle) with a ray that nominally intercepts 'Microlens 2' and is captured by 'True px' on the sensor. Relay blur has the effect of bleeding the ray energy to adjacent pixels ('Bled px'). The circle of blur has the size $\mathrm{d}s_{\text{bled}}$ that is equaled to the relay system's PSF, which we observed to be generally Gaussian with a standard deviation of σ_{PSF}. When the ray

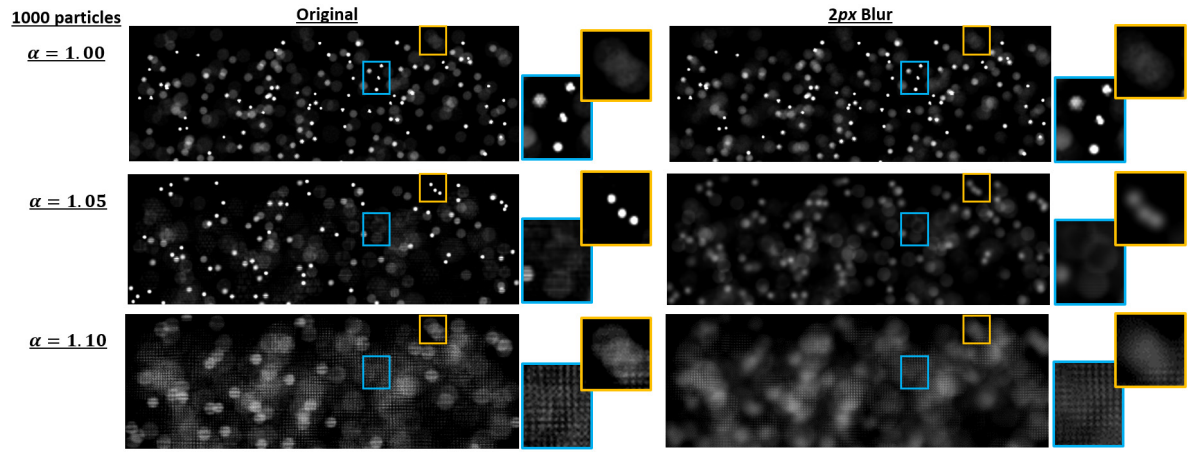

Figure 6. Left: Refocused views of the 1000-particle image. Right: Same views with relay blur applied before refocusing.

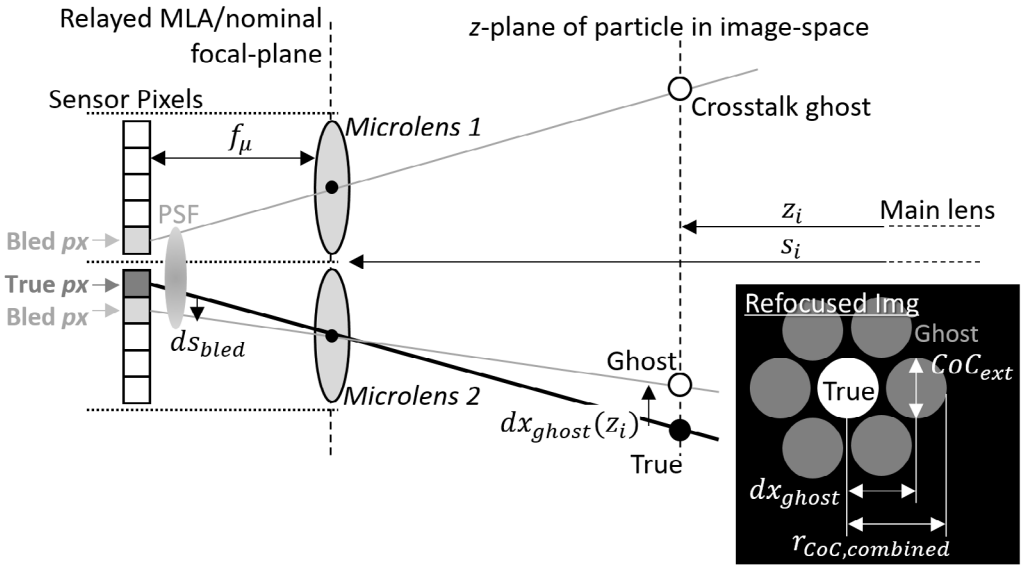

Figure 7. Conceptual model of blurring's impact.

energy (now spread across multiple pixels) is reprojected into the image-space for refocusing, energy in a Bled px produces a fake point ('Ghost') around the 'True' object. As the inset in figure 7 shows, a cluster of ghosts will thus surround the true point, though usually so densely that the ghost and true points are indistinguishable as a blurred circle-of-confusion. We denote the radius of the cluster as $\mathrm{d}x_{\mathrm{ghost}}$, and relate it to $\mathrm{d}s_{\mathrm{bled}}$ via similar triangle:

$$\frac{\mathrm{d}s_{\mathrm{bled}}}{f_\mu} = \frac{\sigma_{\mathrm{PSF}}}{f_\mu} = -\frac{\mathrm{d}x_{\mathrm{ghost}}}{(s_i - z_i)}. \tag{3}$$

Equation (3) can be rearranged to

$$\mathrm{d}x_{\mathrm{ghost}} = -\frac{\sigma_{\mathrm{PSF}}}{f_\mu}(s_i - z_i). \tag{4}$$

Written in terms of main lens focal length f_m, α and system magnification (M):

$$\mathrm{d}x_{\mathrm{ghost}} = -\sigma_{\mathrm{PSF}}\frac{f_m}{f_\mu}(1 - M)(1 - \alpha). \tag{5}$$

These equations suggest that the ghost cluster's radius is proportional to (i) the PSF radius, (ii) the main-lens to microlens focal lengths ratio, and (iii) distance between the real and refocus image planes.

As an added consideration, we note that a plenoptic camera has an *extended* but not an infinite DOF [25]. Particles that are out of focus have a small but finite circle-of-confusion (CoC). Hence, figure 7's inset shows the refocused True and Ghost images as being finite-size circles with the diameter $\mathrm{CoC}_{\mathrm{ext}}$. Thus considering $\mathrm{CoC}_{\mathrm{ext}}$, the full radius of the true and ghost dot-cluster is

$$r_{\mathrm{CoC,combined}} = \mathrm{d}x_{\mathrm{ghost}} + \frac{1}{2}\mathrm{CoC}_{\mathrm{ext}}. \tag{6}$$

The equation above only considered the spread of rays that remain within the same microlens as True px. However, along the edges of the microlens, blurring inevitably causes energy bleed into neighboring microlenses, where they will be reprojected in the opposite of true angle during refocusing, creating a point ('Crosstalk Ghost') that is located very far from the

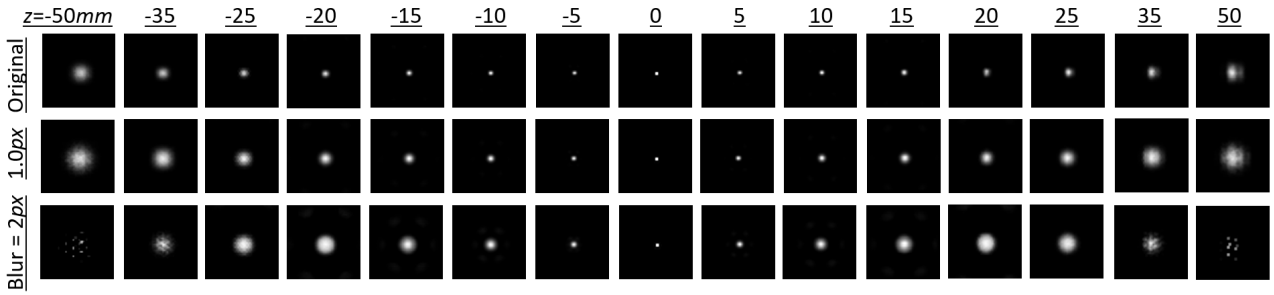

Figure 8. Quality of refocused particles as a function of depth and degree of blur. $z = 0$ at the nominal focal-plane.

ghost/true cluster. For now, we will not model the crosstalk ghosts since rays that cross into neighboring microlenses are proportionately fewer than rays remaining within the same microlens.

The model in figure 7 was tested using synthetic images of point light sources located at different depths within $z = \pm 50$ mm. The images were refocused to each point's physical depths, and the diameters of the refocused points (i.e. their sharpness) were measured. Five levels of blurring from non-blurred to 2.0 px Gaussian kernel were used to test the model. For illustration, examples of the refocused points are shown in figure 8 for the Original synthetic image and two levels of blur. As depths extended beyond ± 20 mm the refocused dot's diameter began to grow even for 'Original' due to the plenoptic camera's finite DOF. The range of z where the refocused dots remained sharp was noticeably narrowed as blurring increased (i.e. reduction of DOF). In fact, at 2 px, no dot could be construed beyond ± 35 mm.

Comparisons of diameters predicted by the model and measured via synthetic images are plotted in figure 9. $\mathrm{CoC}_{\mathrm{ext}}$ was subtracted from the measurements such that only $\mathrm{d}x_{\mathrm{ghost}}$ is assessed. The model and simulation agreed reasonably within the range of ± 20 mm. The 1.5–2.0 px cases have unusually large $\mathrm{d}x_{\mathrm{ghost}}$ values at $z = -5$ mm, because crosstalk ghosts (see insets) were created that bordered and were indistinguishable from the main ghost/true cluster. Beyond $z = \pm 20$ mm, particle quality degraded significantly especially for highly blurred cases since ray energies could not be correctly focused (e.g. see bottom row in figure 8). Hence, the dots could not be accurately segmented from the background, and the measured diameters at extreme depths appear artificially low.

Summarily, analyses based on synthetic images and theoretical models thus far suggest relay blurring bleeds ray energy between pixels, which produces a constant error in reprojection angles that causes increasing spatial errors with refocusing distance.

3.2. The effects of relay blur on 3D reconstruction

Section 3.1 elucidated the impact of relay blur on refocused images. This section demonstrates that a similar impact extends to 3D reconstruction. Figure 10 contains iso-contour plots of a reconstructed volume containing 1000 particles. The figure is shown in top-down projection where z is aligned with the optical axis (i.e. view flattened in y). Five reconstructions of the same particle field, one original and four blurred, are

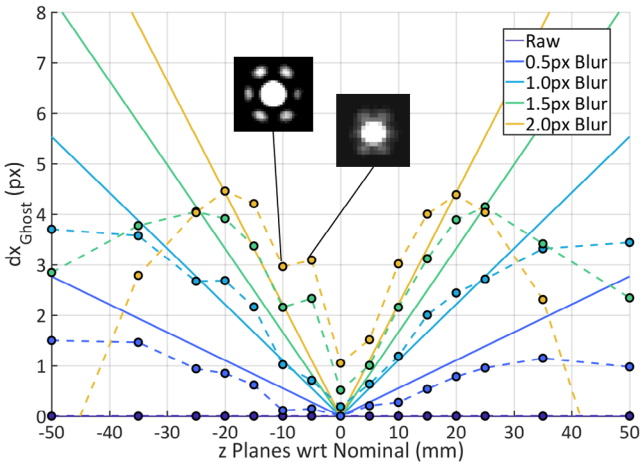

Figure 9. Comparison of the analytical blurring model (solid lines) against particle diameters measured from simulation (dashed lines).

shown. The iso-contour of each plot has been adjusted such that particles along the nominal focal-plane are approximately the same size across all cases.

We observe that the reconstructed particles near the nominal focal-plane are rounder in all cases, while particles on both sides are more elongated. This is a known characteristic of 3D reconstruction based a single plenoptic camera, caused by the narrow angular range of a monocular lens [12]. In contrast, a new phenomenon is observed where the spread of particles appears to narrow towards the nominal focal-plane when blurring increased (e.g. the Original case spans $z = -22$ to 22 mm whereas the 2.0 px Blur case only spans $z = -5$ to 5 mm). Though not evident from figure 10 alone, particles at extreme depths did not disappear, but simply became too softly-focused and dim to show up above the iso-contour level.

Quantification of the phenomenon in figure 10 is performed via the measure of 'slice-wise normalized intensity variance' ($\widetilde{\sigma}^2_{E,\mathrm{slice}}$). First employed by Novara and Scarano [26] to characterize the SNR of reconstructed particle fields, the normalized intensity variance is defined as

$$\widetilde{\sigma}^2_E \equiv \frac{\sqrt{\frac{1}{N_{vx}} \sum_{i=1}^{N_{vx}} \left(E_i - \overline{E}\right)^2}}{\overline{E}} \tag{7}$$

where E_i is the intensity of a particular voxel, $\overline{E}$ is the global average and N_{vx} is the set of voxels within the volume. An $\widetilde{\sigma}^2_E$ of 20–30 is typically indicative of acceptable SNR [27]. Since we are concerned about the distribution of SNR as a function

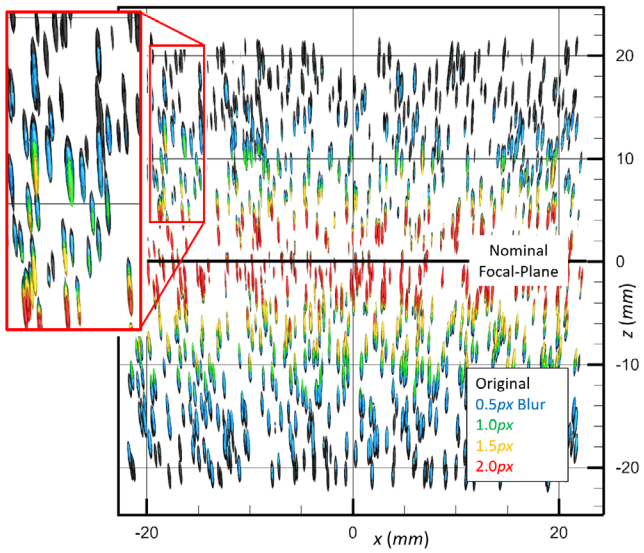

Figure 10. Top-down view of reconstructed 3D particles-fields for the 1000-particle case with different degrees of blur.

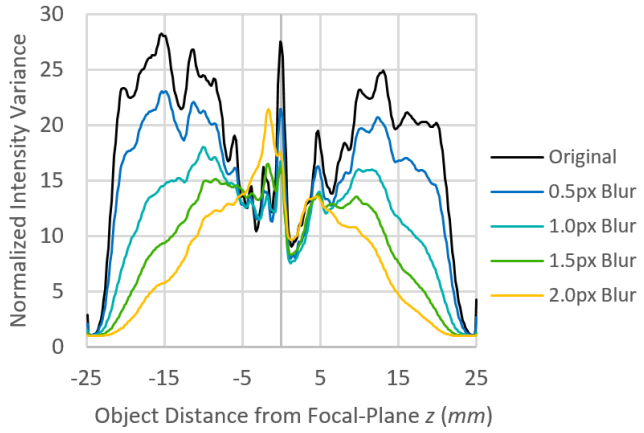

Figure 11. The effect of blurring on the reconstructed volume's $\widetilde{\sigma}^2_{E,\text{slice}}$ for the 1000-particle case.

of z, a new parameter $\widetilde{\sigma}^2_{E,\text{slice}}(z)$ is employed, where the variance is calculated across constant-z slices.

Figure 11 shows the effect of blurring on $\widetilde{\sigma}^2_{E,\text{slice}}$. Consistent with common plenoptic characteristics [12], the Original case contains a sharp $\widetilde{\sigma}^2_{E,\text{slice}}$ peak at the nominal focal-plane. The regions immediately next to this peak and at the volume's extremities have low $\widetilde{\sigma}^2_{E,\text{slice}}$. The region around ± 15 mm contains two broad humps of relatively high $\widetilde{\sigma}^2_{E,\text{slice}}$. It is evident from figure 11 that as blurring increased, $\widetilde{\sigma}^2_{E,\text{slice}}$ decreased significantly. The effect is most pronounced near the extremities of the volume and is least felt near the nominal focal-plane, i.e. consistent with the observed DOF-reduction due to blurring in refocused images. Similar trends as figure 11 were observed for all tested particle densities.

While $\widetilde{\sigma}^2_{E,\text{slice}}$ assessed the volume's SNR distribution, we can also assess the *accuracy* of reconstruction using the measure of quality (Q) factor. First introduced by Elsinga

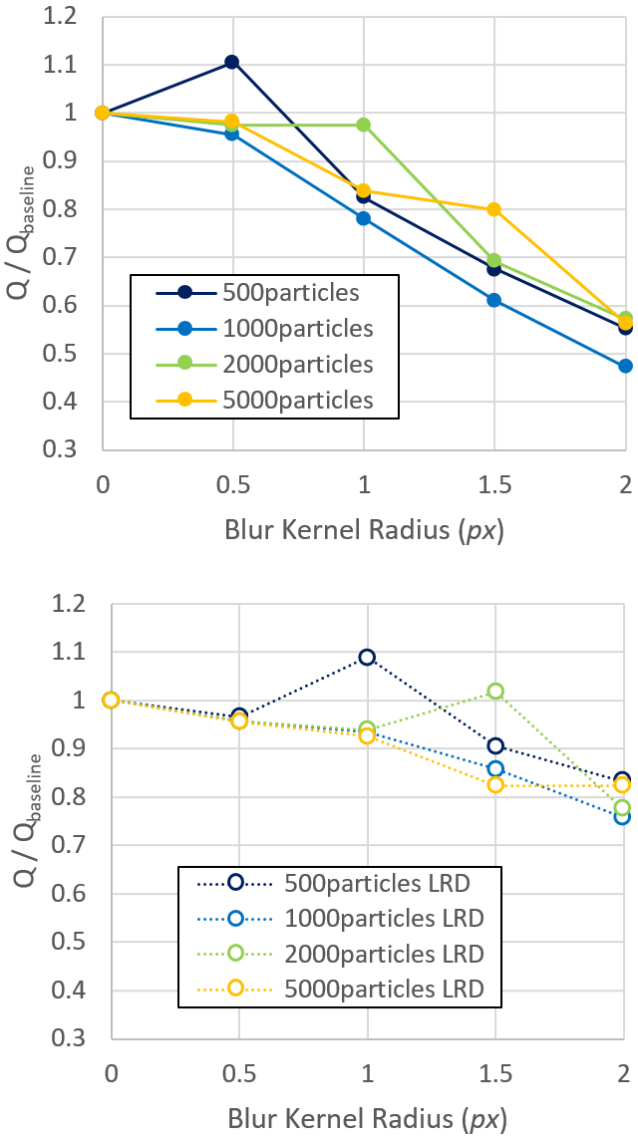

Figure 12. The effect of blurring on the reconstructed volume's Q-factor. Top: Reconstruction based on Original and blurred cases. Bottom: Reconstruction after blurred images were pre-processed with LRD (points at 0 px blur are placeholders only).

et al [28] and later modified by La Foy and Vlachos [29], it is defined as

$$Q \equiv \frac{\sum_{x,y,z} \widetilde{E}_{\text{recon}}(x,y,z) \cdot \widetilde{E}_{\text{true}}(x,y,z)}{\sqrt{\sum_{x,y,z} \widetilde{E}^2_{\text{recon}}(x,y,z) \cdot \sum_{x,y,z} \widetilde{E}^2_{true}(x,y,z)}}$$

where $\widetilde{E}$ is the volume's mean-subtracted voxel intensities. The Q-factor evaluates the degree of correlation between the known true-field ($\widetilde{E}_{\text{true}}$, which was synthesized by placing a small Gaussian-intensity sphere in the voxels where particles are known to reside) and the reconstructed volume ($\widetilde{E}_{\text{recon}}$).

The top of figure 12 shows Q-factors (normalized by the baseline non-blur case) as a function of blur and particle densities. While Q-factors are known to suffer at very high densities for both plenoptic and regular four-camera tomography, no dependence is observed within the sparse to moderately dense

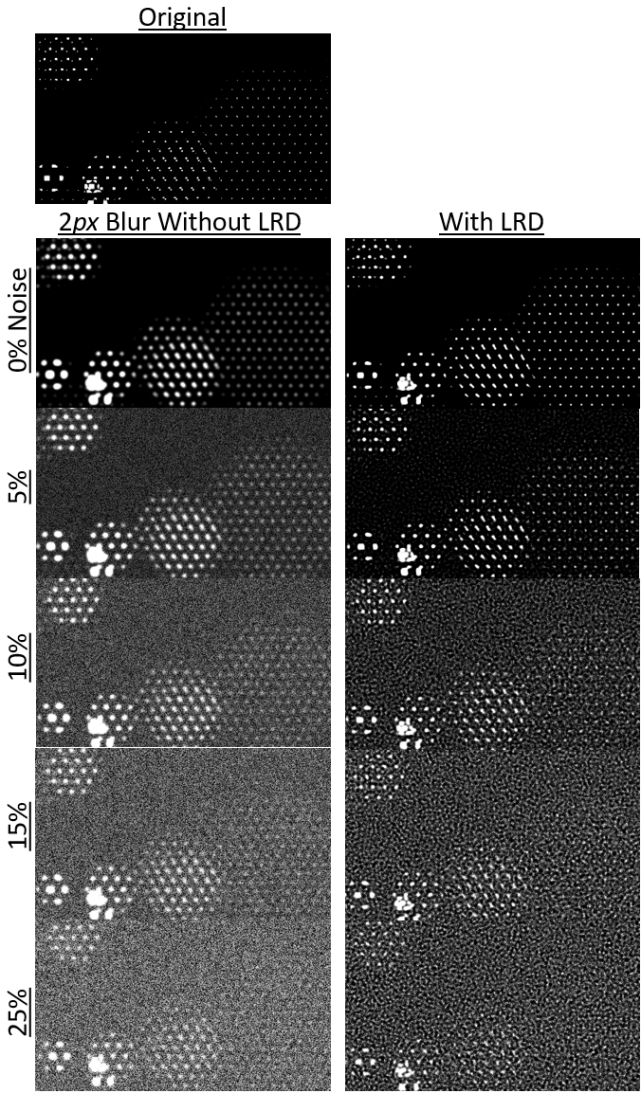

Figure 13. Results of LRD performed on an image blurred by 2 px Gaussian PSF, with different intensities of random noise. Noise% indicates the maximum intensity of added noise relative to maximum particle intensity. 1000-particle case shown.

tested cases. In contrast, the Q-factors dropped steadily with blurring, down to as low as 50%–60% of baseline with 2 px of blur. This trend suggests relay blur displaces reconstructed particles from their true positions (i.e. lowering accuracy) *in addition* to lowering SNR at extreme depths. Qualitatively, this interpretation can be supported with the inset of figure 10 where particles can be seen drawn towards the nominal focal-plane when blurring increase.

Interestingly, figure 12 shows the 500-particle volume with 0.5 px of blur outperforming its non-blur counterpart by ~10%. This is potentially because while reconstructed particles in the non-blur baseline are sharp, they may be just sufficiently misaligned against the ground truth to impact Q-factor value (due to elongation and other errors associated with single-camera reconstruction). Small amounts of blur in the image may increase reconstruction-truth overlap (i.e. Q-factor) by blurring/enlarging the reconstructed particles.

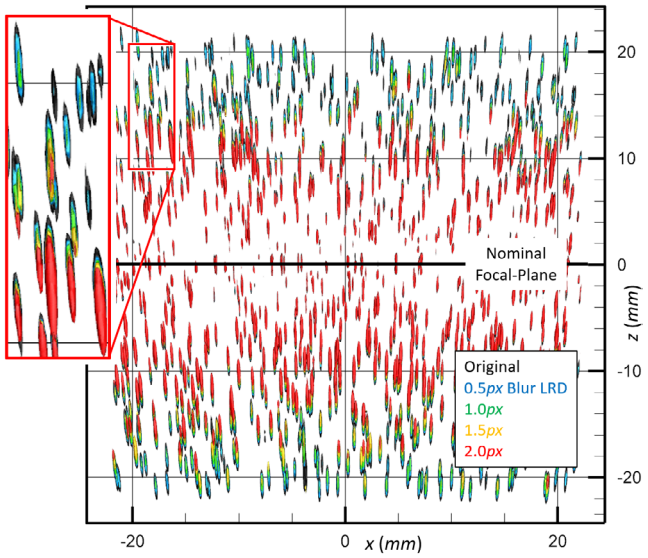

Figure 14. The impact of LRD on the reconstruction of 1000 particles. See figure 10 for non-LRD counterpart.

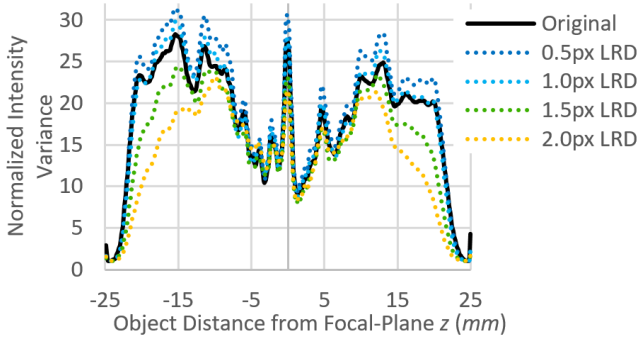

Figure 15. The effect of applying LRD on $\widetilde{\sigma}^2_{E,\mathrm{slice}}$ for the 1000-particle case. See figure 11 for non-LRD counterpart.

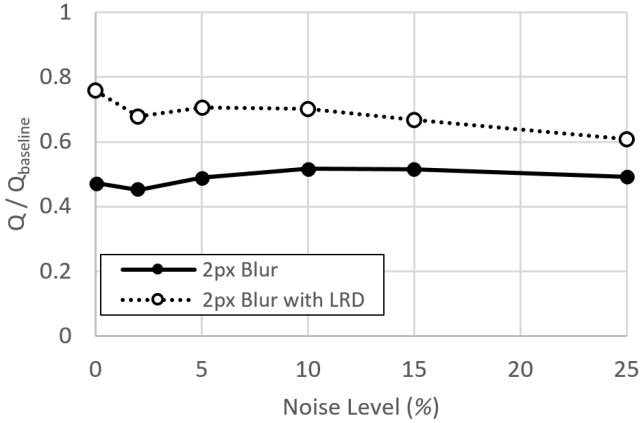

Figure 16. The effect of noise on Q-factor of the 1000-particle, 2 px blur case (normalization against non-blurred original).

3.3. Implementation of the LRD procedure

The process of imaging can be described as a convolution of the imager's PSF with the physical light-field. In this study, we attempt to reverse the relay blur through sharpening the

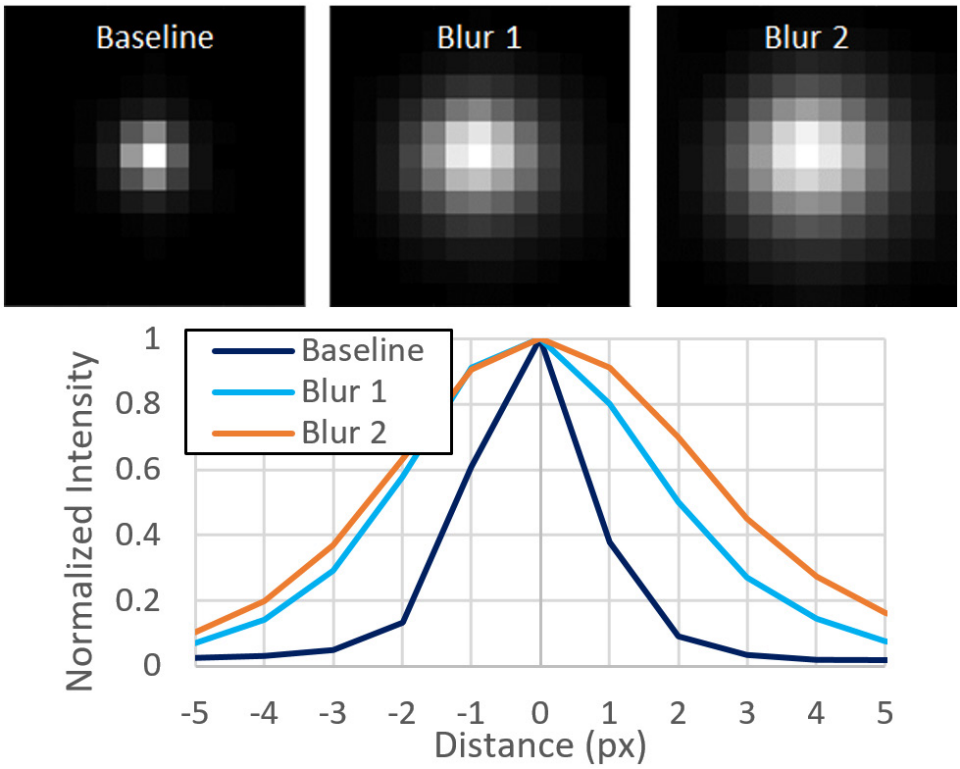

Figure 17. Approximate PSF of the relay system under the baseline and de-tuned conditions.

raw plenoptic image via the classical LRD. LRD was first developed to sharpen astronomical images [30, 31] and has since made its way to standard imaging toolboxes [32]. In many circumstances, LRD provides results that are superior to simpler sharpening tools such as Unsharp Mask through leveraging known information about the system's PSF. In plenoptic imaging, we have the convenient situation where the image of dots acquired during MLA calibration (see figure 5) naturally characterizes the PSF of the relay lens. Hence, the LRD procedure to sharpen plenoptic images consist of (i) extracting a sample batch of all PSF dots from a calibration image such as figure 5, (ii) averaging the samples to approximate a global PSF, (iii) performing LRD on the image with this PSF. Notably, deconvolution procedures such as LRD typically suffers from imaging noise, which is prevalent within real intensified and PPIV images. Hence, in addition to blurred synthetic images, we also tested LRD on images with different degrees of synthetic salt-and-pepper noise.

Figure 13 shows the zoomed-in results of LRD performed on a particle image with 2 px of Gaussian blurring followed by different levels of noise. Comparing the Original against the 0% Noise row, we qualitatively observe that the simulated blurring was noticeably reversed in the absence of noise, i.e. the blurred dots shrunk, and the post-LRD image more closely resembles the Original. Adding noise degraded the LRD results: the achievable amount of image sharpening does not appear to be significantly affected (e.g. the leftmost clusters in each image appear similarly sharp at all noise levels), but bright macroscopic-scale dots are formed by LRD out of the initially dim pixel-scale noise speckles in the background. The brighter large-scale noise post-LRD decreases our ability to discern the correct particle clusters.

Figure 14 shows the effect of LRD on particle field reconstruction, using the same image from figure 13, with different degrees of blurring and the absence of noise. Like figure 10, iso-contour levels were chosen to match particle size near the nominal focal-plane. Comparing figures 10 and 14, we observe that reconstruction based on post-LRD images noticeably mitigated the DOF-reduction impact of blurring, i.e. reconstructed particles from blurred cases now remain visible further out from the nominal focal-plane. Quantitative comparison is made using the $\widetilde{\sigma}^2_{E,\text{slice}}$ plots in figures 11 and 15. Where blurring significantly reduces $\widetilde{\sigma}^2_{E,\text{slice}}$ in the far $\pm z$ region, LRD successfully recovered most of the lost $\widetilde{\sigma}^2_{E,\text{slice}}$ values. For example, at $\leqslant$1 px worth of blur, all of the Original case's $\widetilde{\sigma}^2_{E,\text{slice}}$ values are recovered. Similarly, the previously shown figure 12 compares Q-factor values for blurred cases with and without LRD at various particle densities. Whereas 40%–50% of losses in Q-factor were experienced at 2 px blur pre-LRD, we observe only 20%–25% of losses post-LRD. Once again, no dependence on particle densities is observed. The findings thus far suggest LRD is effective at mitigating relay blur in the absence of noise. In contrast, the Q-factor plots in figure 16 (based on 1000-particle images of figure 13) suggest noise has a noticeable but otherwise mild impact on the accuracy of the reconstructed volume. Recovery of volume accuracy through LRD was achieved up to fairly severe (25%) noise levels.

Summarily, synthetic image results in section 3 showed that relay blur on raw plenoptic images has a blurring effect

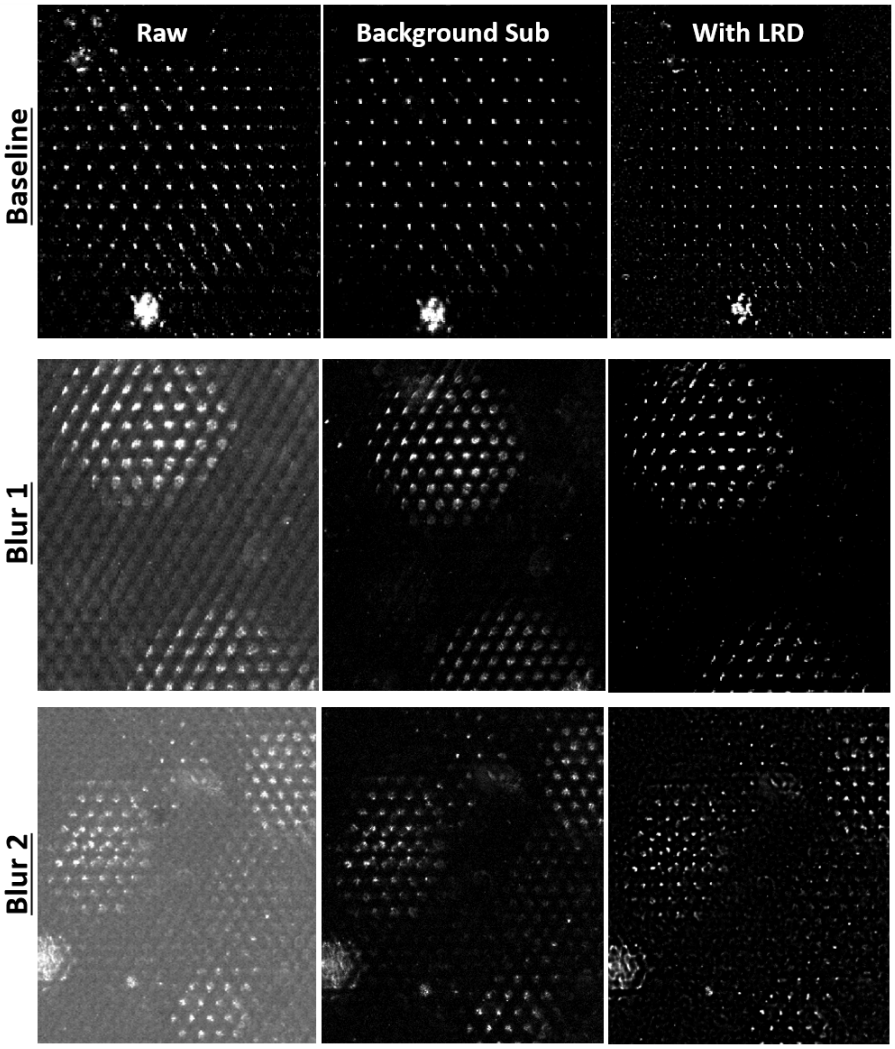

Figure 18. Left: Raw experimental images; center: post-processed images without LRD procedure; right: with LRD.

on refocused image which grows linearly with refocusing distance. Physically, this is caused by inter-pixel ray energy bleed during relay blurring, which imposes a constant angular error in ray reprojection during refocusing. At constant angular error, the spatial errors of reprojected rays increase with distance. Consequently, relay blur reduces the system's effective DOF and in the case of 3D particle reconstruction, hampers the ability to reconstruct particles at extreme depths. LRD was found to be effective at mitigating relay blur, resulting in improved reconstruction SNR *and* accuracy. The procedure was, however, sensitive to image noise.

4. Results and analysis (experimental image)

4.1. Validation of relay blur's impact and the LRD method

Three test cases were performed with the relayed high-speed camera system in figure 2: a baseline case with the system tuned for the sharpest image, as well as two cases where the relay lens was deliberately defocused to simulate blurring due to maladjustments or lens aberration. The system's measured PSF's under these conditions are shown in figure 17. For the baseline case, $\sigma_{\text{Baseline}} = 0.87$ px, while for the detuned cases $\sigma_{\text{Blur 1}} = 1.92$ px and $\sigma_{\text{Blur 2}} = 2.36$ px, i.e. the detuned cases were representative of the worst cases in our synthetic data, while the baseline case was in the mid-range. Notably, the PSF's in figure 17 are approximations, because they do not consider spatial dependence of aberrations, and because the spot size of the closed aperture is estimated to be 1.56 px instead of single-pixel impulse.

Zoomed-in views of the raw plenoptic images are shown on the left column of figure 18. Particles far from the nominal focal-plane appear as large clusters of point-like dots in the Baseline case, as is expected for a sharp plenoptic image. Similar dots are noticeably blurred to finite sizes in Blur 1 and Blur 2's raw images. Images were captured with settings that barely saturate the brightest particles to make use of the camera's full dynamics range. With respect to this full dynamic range, background noise-levels for Baseline is 2.6%, while that of Blur 1 is 5.7% and Blur 2 is 7.3%. Exact particle count is hard to obtain due to image noise; however, an approximate particle density of 450 particles per image (i.e. 0.01 particle per microlens) is estimated, which is similar to densities in the 1000-particle synthetic image. Notably, the main-lens

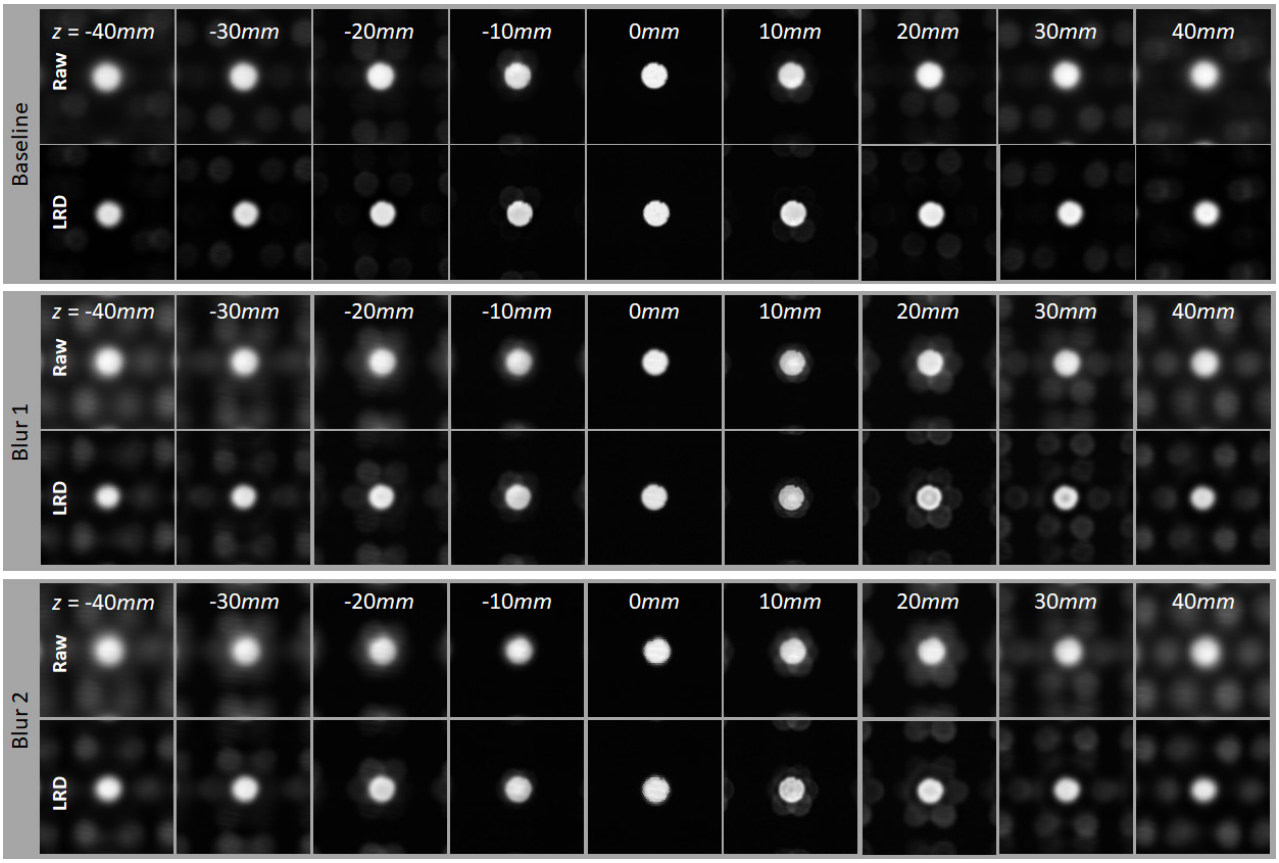

Figure 19. Calibration dots refocused at their physical depths, elucidating the effect of blurring and LRD on the depth-dependent refocusing sharpness. Centermost dot on plate shown.

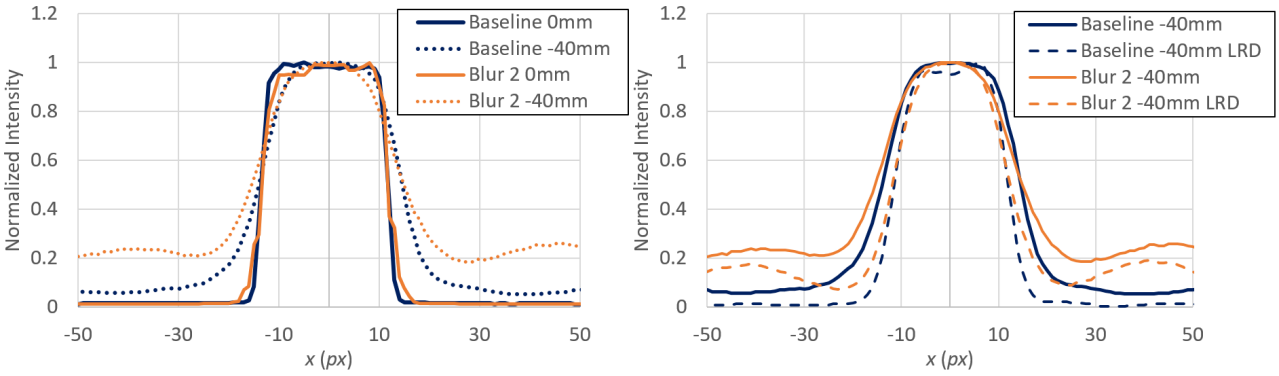

Figure 20. Plots of normalized intensity profiles across dots in figure 19, with and without LRD.

magnifications of the experimental images were maintained from −0.495 to −0.505, close to the synthetic image's −0.5 to make both datasets comparable. For illustrative comparison, the center and right columns of figure 18 represent the same views with plain background subtraction and with LRD, respectively.

The impact of relay blur on refocusing is characterized through images of the calibration dot-plate. As described in section 2, the dot-plate was translated from $z = -40$ to 40 mm and imaged at every 10 mm increment. Figure 19 shows views of the centermost dot at every imaged location. The refocus plane in each view coincides with the physical location of each dot when it was recorded. Along the centermost column, we note that dots have similar sharpness between Baseline, Blur 1 and Blur 2 when $z = 0$ mm, i.e. consistent with earlier findings, subjects near the camera's nominal focal-plane are least sensitive to relay blurring. Similarly, the leftmost and rightmost columns of the 'Raw (non-LRD)' views show that relay blurring significantly degraded image sharpness at off-nominal depths. For example, the Baseline/Raw/40 mm image is significantly sharper than Blur 2/Raw/40 mm. These observations are quantitatively expressed on the left of figure 20: plots of intensity distributions across the dot show that differences between Baseline and Blur 2 are only evident at off-nominal z.

In further agreement with previous findings, 'Crosstalk Ghost' (see figure 7) manifested within figure 19. For example, the background region in the $z \sim 0$ mm planes are relatively clean for all cases. However, at $z \geqslant \pm 20$ mm faint secondary crosstalk ghost dots began to surround the true dot.

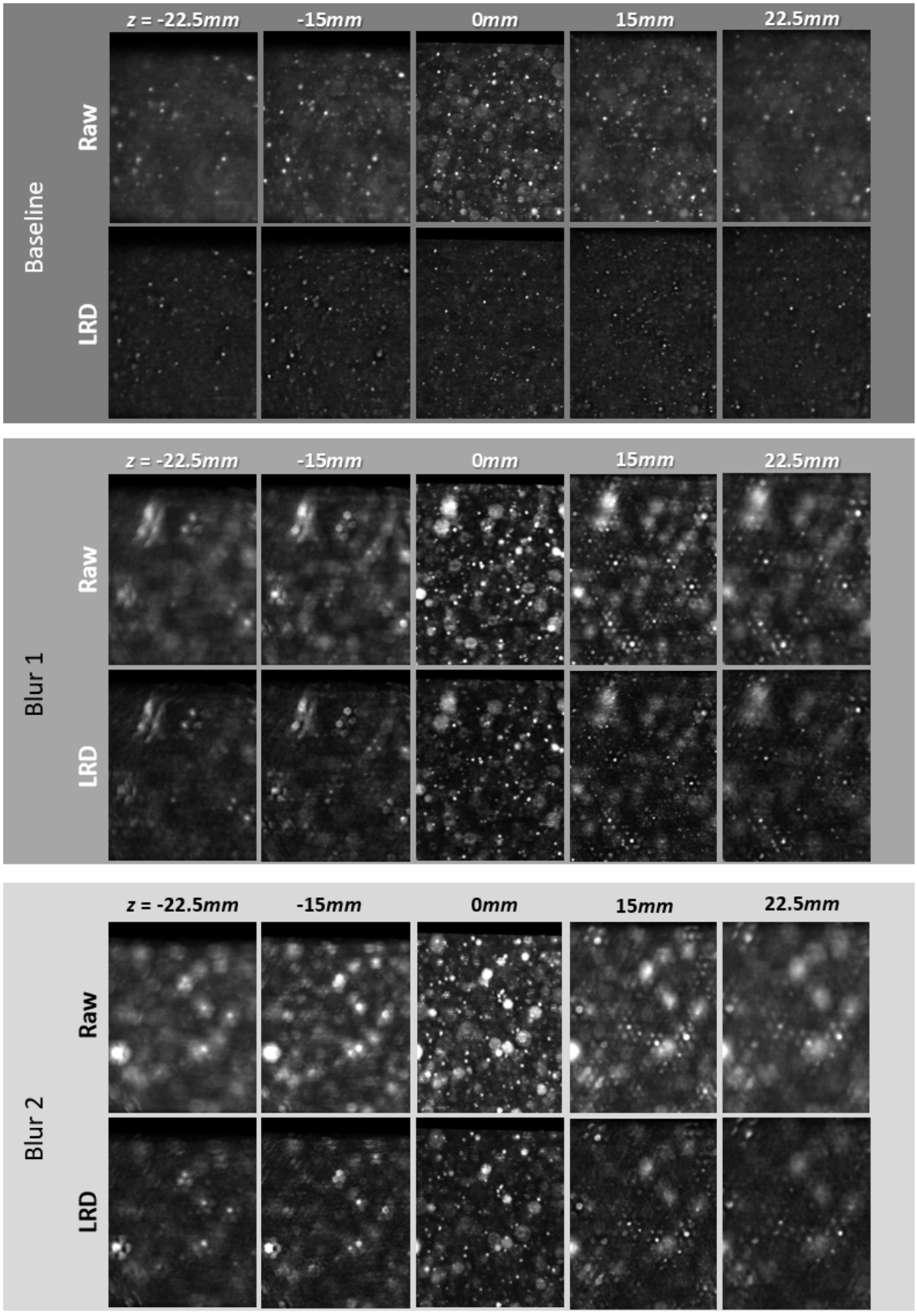

Figure 21. Refocused particle-fields (cropped center 1/3 of full image) with and without LRD procedure.

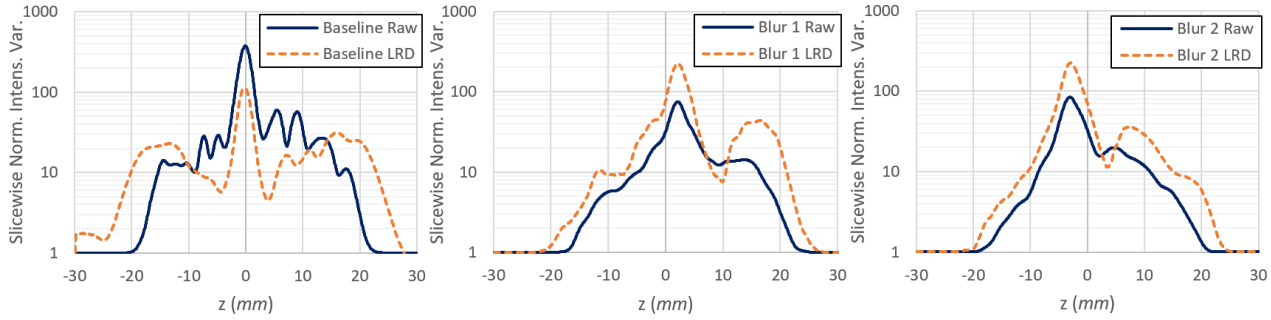

Figure 22. $\widetilde{\sigma}^2_{E,\text{slice}}$ distributions under the influence of varying blur and LRD. Data based on the average of 50 images.

Separation between these ghosts and the true dot increased with refocusing distance, similar to what was observed in figure 9. The manifestation is particularly prevalent for Blur 1 and Blur 2 images, which is to be expected since crosstalk ghosts result from energy bleed between adjacent microlens. Notably, six crosstalk ghosts appear in our data due to the hexagonal MLA that we employed. Ghost intensities can also be observed in figure 20 through the high background intensity at Blur 2/− 40 mm.

The application of LRD using PSF's approximated from figure 17 successfully improved the refocused images' sharpness and suppressed ghost intensities in all cases, as evident from figure 19. Furthermore, the influence of LRD was more pronounced for Blur 1 and 2 than for the initially sharp Baseline. This can be observed from the right side of figure 20 where the Baseline $z = -40$ mm dot shows a small degree of sharpening due to LRD (i.e. narrower top-hat profile and background intensities closer to true-black), while Blur 2's profile narrowed more significantly. The background regions in Blur 2 still contains some ghost intensities, but at lower values compared to non-LRD data. Results from figures 19 and 20 lend us confidence that trends deduced from synthetic images and theory are both translatable to experimental data.

Where figures 19 and 20 assess blurring and LRD's impact on refocusing, figures 21 and 22 look at 3D particle fields in a PPIV scenario. Since particle distribution is necessarily not as uniform and controlled in experiment, the statistics in this section's analysis is based on the average of 50 images in each case. Figure 21 shows the instantaneous particle image refocused to five different depths, ranging from the nominal focal-plane to the extremes of the illuminated volume. Intensities in these images have been scaled from 0% to 50% of each case's global maximum. At the $z = 0$ mm depth, refocused images from Baseline, Blur 1 and 2 appear similarly sharp (i.e. the smallest/in-focus particles are similarly point-like). However, based on our intensity-scaling, the Blur 1 and 2 images are both contain brighter large dots than the Baseline. This is likely because small amounts of blurring prevented particles (especially nominal focal-plane particles) from being focused into extremely bright infinitesimal points, i.e. the dynamic range between focused and out-of-focus particles is smaller in the presence of blurring, hence the overall image of in- and out-of-focus particles appear brighter in Blur 1 and Blur 2.

Point-like particles continue to be present in the Baseline case's off-nominal planes. In contrast, significant blurring and

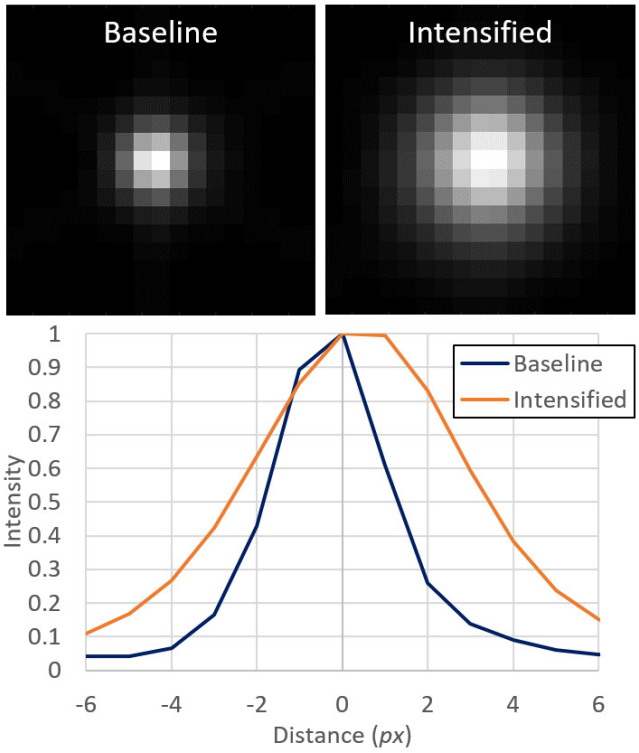

Figure 23. PSF of the baseline and intensified relayed-plenoptic camera system.

distortion appear in the Blur 1 and 2 images. Interestingly, particles in the negative and positive z ranges appear differently distorted in figure 21. Particles at positive z appear sharp and contain well-defined six-point crosstalk ghosts, while particles at negative z are blurred into hexagonal patterns without very noticeable ghosts. This behavior is somewhat different from synthetic images where blurring on both sides of the nominal focal-plane behaved similarly, which suggests real relay blurring may differ slightly from the anisotropic blurring simulated on the synthetic images. The application of LRD to these images appear to suppress the intensity of ghosts and the background's blurry glow, thus improving the true particles' SNR. The application of LRD also raises the dynamic range of in-focus versus out-of-focus particles near $z = 0$ mm, evident from the dimmer appearance of all $z = 0$ mm cases.

MART was performed on the experimental images to reconstruct the 3D particle fields. $\widetilde{\sigma}^2_{E,\text{slice}}$ is then used to assess the z-dependent SNR of the reconstructed volumes. Similar

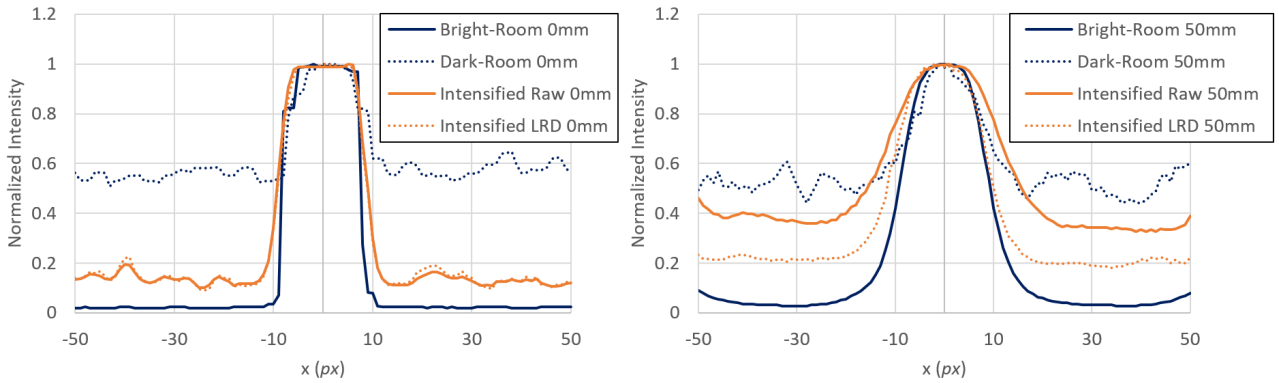

Figure 24. Plots of normalized intensity profiles across the centermost calibration dot under different imaging settings.

to volumes reconstructed from synthetic image (figure 11), the $\widetilde{\sigma}^2_{E,\text{slice}}$ curve of the Baseline experimental volume (see leftmost plot in figure 22) contain a $\widetilde{\sigma}^2_{E,\text{slice}}$ peak at $z = 0$ mm. The $\widetilde{\sigma}^2_{E,\text{slice}}$ values then range between 20–75 on both sides of the focal-plane before falling to zero slightly shy of ± 20 mm (short of the full illuminated depth of ± 22.5 mm). Applying LRD suppressed the unusually high $\widetilde{\sigma}^2_{E,\text{slice}}$ peak at $z = 0$ mm, while pushing the region of non-zero $\widetilde{\sigma}^2_{E,\text{slice}}$ out towards the full volume depth. The characteristic $\widetilde{\sigma}^2_{E,\text{slice}}$ humps on both sides of the $z = 0$ mm plane (e.g. at $z = \pm 15$ mm in figure 11) also manifested in figure 22's baseline data after LRD was applied.

Notably, even after LRD was applied the $\widetilde{\sigma}^2_{E,\text{slice}}$ peak at $z = 0$ mm remained significantly broader in the experimental data compared to synthetic, i.e. more energies are 'anomalously' concentrated around the nominal focal-plane in experiment. This is likely attributable to pixel blooming/saturation in the experimental images, i.e. photon energies from very bright particles near the nominal focal-plane spill over to adjacent pixels on a real camera (e.g. see the bright small cluster at the bottom of figure 18's top-row), compared to synthetic data where this imperfection is absent (e.g. leftmost small cluster in figure 3). The spill-over results in incorrectly large particles near the nominal focal-plane, which deposits incorrectly large amount of energy around the $z = 0$ mm region of the volume.

In the same manner in which small amounts of blurring reduced the in-focus versus out-of-focus particles' intensity disparity (see figure 21), we observe the that the $\widetilde{\sigma}^2_{E,\text{slice}}$ curve in the Blur 1 and Blur 2 cases are significantly less peaky than the Baseline case. Additionally, consistent with observations in figure 21 that particles on the positive z side appear sharper in the Blur 1 and 2, $\widetilde{\sigma}^2_{E,\text{slice}}$ values on the positive z side also appear higher in figure 22. Interestingly, detuning the relay lenses appear to shift the peak $\widetilde{\sigma}^2_{E,\text{slice}}$'s location away from the Baseline case's $z = 0$ mm position, further suggesting real relay blurring may not be as straightforward as anisotropic blurring and further investigation may be warranted. Finally, the Blur 1 and Blur 2 cases' $\widetilde{\sigma}^2_{E,\text{slice}}$ magnitudes are approximately identical, reflecting their similar PSF. Applying LRD increased $\widetilde{\sigma}^2_{E,\text{slice}}$ values of the blurred cases globally, including around the $z = 0$ mm depth. The $\widetilde{\sigma}^2_{E,\text{slice}}$ hump normally located $\approx$15 mm away from the peak manifested after LRD was applied, but only on the positive z side.

From this investigation, it is shown that LRD results in volumes that resemble the ideal synthetic data when the level of blurring is mild (i.e. the Baseline case). For severely blurred cases (Blur 1 and 2), SNR in regions far from the nominal focal-plane were only partly recovered. It remains to be investigated whether the post-LRD Blur 1 and 2 volumes are sufficient to support accurate 3D PIV calculations.

4.2. Application of LRD method to intensified plenoptic imaging

The current findings and LRD procedure were applied to intensified plenoptic imaging using figure 2's system. The intensified system was used to image a calibration dot-card (5 mm dot-spacing and ~1 mm dot diameter). For baseline comparison, a non-intensified relayed plenoptic system with the same relay and microlens array was also deployed to image the same target. Main-lens magnification on both systems were near-identical ($M = -0.304$ to -0.307), at which the theoretical maximum DOF was ~100 mm. The baseline camera was used to image the dot-card in a brightly-lit room, and also at 50% camera gain, 250 μs exposure in a dark-room where the dot-card was barely visible. The intensified system was then used to image the dot-plate in the same dark-room, also under 50% gain and 250 μs exposure. The level of intensification was set to 800 V on the micro channel plate (out of a maximum of 900 V). Figure 23 shows the approximate PSF of the baseline and intensified system. $\sigma_{\text{Baseline}} = 1.40$ px (similar to earlier results) while $\sigma_{\text{Intensified}} = 2.74$ px, which is notably lower than the on-paper lp/mm value.

Figure 24 compares the sharpness of the centermost dots at the nominal focal-plane and $z = 50$ mm, refocused to their respective depths. Under the brightly-lit non-intensified condition ('Bright-Room'), intensity profile across the 0 mm dot is nearly perfectly square; i.e. very sharp image. At 50 mm the corresponding dot is noticeably blurrier with more rounded intensity profile. Background noise-levels were in the <5% range for both depths. In 'Dark-Room', the non-intensified system has similar sharpness at both depths. However, background noise-level is significantly higher (50%–50% of peak intensity). By intensifying the image ('Intensified Raw'),

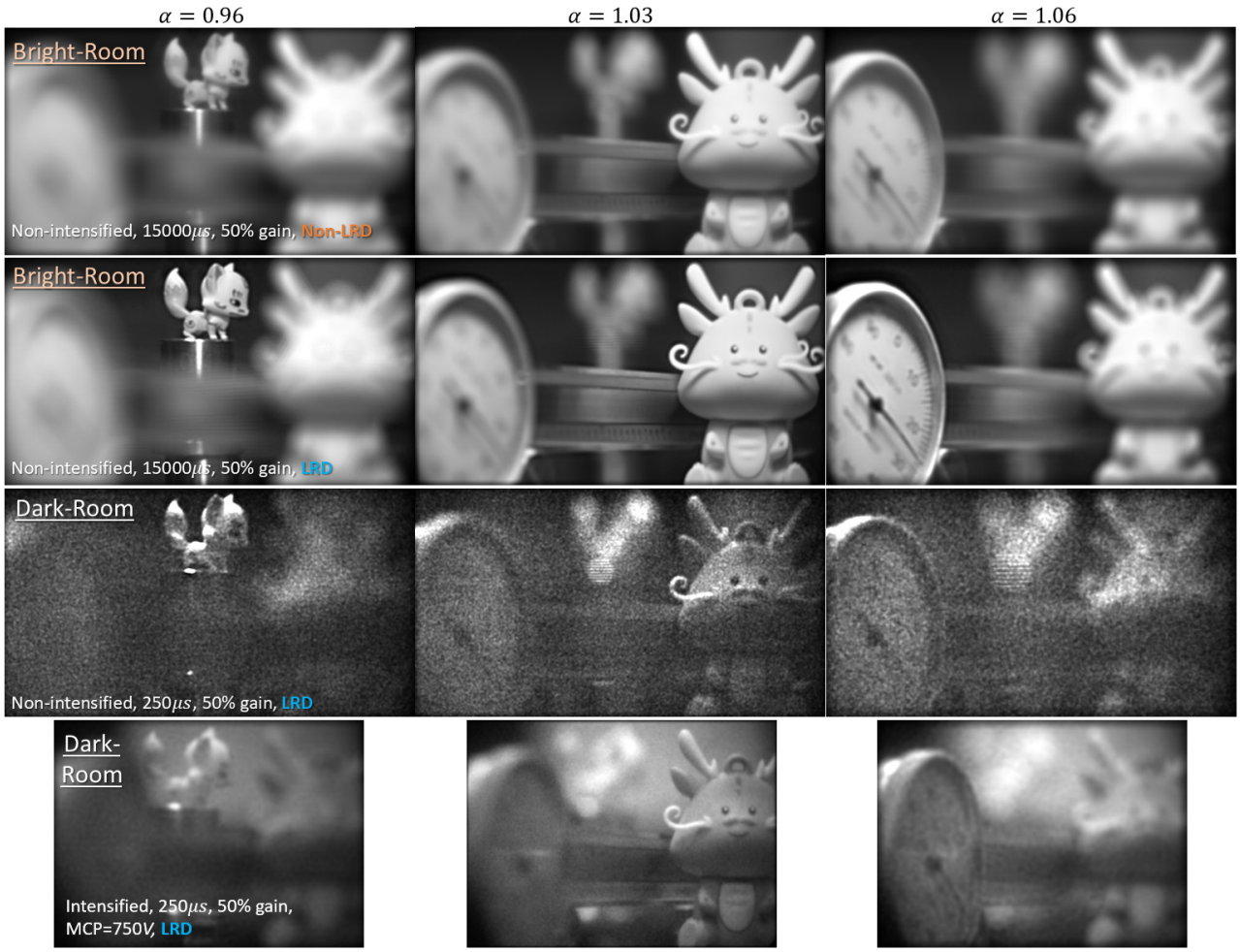

Figure 25. Demonstration of LRD procedure on relayed and intensified plenoptic images.

background noise was reduced to 10%–20% at $z = 0$ mm. Similar sharpness as Bright-Room was also achieved. However, at $z = 50$ mm, Intensified Raw contained ~40% background noise-level and the intensity profile was very broad (i.e. blurred dot). This is consistent with previous findings where blurring of the raw image (in this case due to the low-resolution intensifier) has an impact that is exacerbated by depths. Similarly, the application of LRD ('Intensified LRD') did not affect the 0 mm image, but significantly improved image sharpness and background noise-level at 50 mm. These results thus suggest that under dim-light or UV/IR light conditions where a normal camera's intensities are near-zero, intensified plenoptic can achieve substantially higher image-quality than non-intensified alternatives, but only after LRD is performed.

Finally, we applied our findings and the LRD procedure to a real-world scene in figure 25. This scene spanned approximately 35 cm in depth, captured with a main-lens magnification of $M_{\text{main}} \approx -0.29$ (theoretical maximum DOF of $\approx$ 17.5 cm). For baseline, this scene consisting of a caliper dial in the foreground, a dragon near the nominal focal-plane and a fox in the background was captured with figure 2's regular relayed-plenoptic camera under brightly-lit condition with 50% camera gain and long exposure. Evidently, details on the fox and caliper dial were not well resolved until LRD was applied, due to a small amount of relay blurring. For example, the dial numbers were only readable after LRD. Under a dark-room, short-exposure condition, the same image became very noisy. Details on the caliper and the bottom-right corner of the dragon are no longer resolved even with LRD. Using identical camera settings, similar lens magnification and perspective, a version of the scene captured with intensifier markedly improved image signal-to-noise ratios. Details such as the bottom-right of the dragon and dark patches of numbers on the dial became better resolved. The practical benefits of LRD and intensification are thus demonstrated through figure 25.

5. Conclusion

Relayed-MLA has been identified as an important architecture for plenoptic cameras, especially for scientific prototyping, high-speed imaging and intensified imaging. However, relay lenses inevitably introduce blurring to the plenoptic image, which was found to have the unintended consequence of significantly reducing the camera's maximum refocusingDOF. In this paper, we formally characterized the depth-dependence of blurring in a plenoptic system, from which a theoretical model was proposed and validated. Subsequently, image sharpening based on LRD was investigated as an approach to partially mitigate blurring introduced by the relay lenses.

Through analysis of synthetic plenoptic images, we observed that blurring at the level of raw image translates to refocused images which are blurred by a degree proportional to $|s_i - z_i|$. Hence, sharpness of objects far from the camera's nominal focal-plane are more highly impacted by blurring, thus effectively reducing the system's DOF. The root cause of this z depth dependence can be linked to the plenoptic camera's approach of encoding ray angle on pixel space, i.e. the blurring of ray energies from one pixel to another on the raw image causes incorrect ray re-projection angle during perspective-shifting and refocusing. Errors in re-projection angle then scales proportionally with re-projection distance ($|s_i - z_i|$).

Analysis of synthetic 3D particle-field images concluded that blurring also impacts the ability to perform 3D tomographic reconstructions for PPIV applications. Notably, the reconstructed intensities of particles far from the nominal focal-plane are significantly reduced by blurring. This observation was verified in experimental particle-field data.

LRD was proposed as a method for mitigating relay blurring. The relay system's PSF required to perform LRD was approximated from a raw plenoptic image taken with the main-lens aperture closed to a minimum (i.e. where the microlenses see a point-like source of light). On all occasions, LRD was able to restore significantly amounts of image sharpness/particle intensities in the regions far from the focal plane. The accuracies of the tomographically reconstructed particle-fields were also markedly improved after LRD. In addition, the LRD approach was found to be particularly beneficial for intensified plenoptic images, where substantial blurring and loss of resolution are inevitable during passage through the intensifier.

Finally, to confine the scope of the investigation, only a plain LRD approach was studied. In future iterations, notable improvements are likely obtainable through the use of more advanced deconvolution approaches such as (i) locally-varying PSF, (ii) switching to blind deconvolution with the measured approximate PSF as the initial PSF.

Acknowledgments

Development of the relayed plenoptic system used in this study was supported by the National Science Foundation's Major Research Instrumentation Program Grant No. 1725929.

ORCID iDs

Zu Puayen Tan https://orcid.org/0000-0003-3668-5198

References

[1] Adelson E H and Wang J Y A 1992 Single lens stereo with a plenoptic camera *IEEE Trans. Pattern Anal. Mach. Intell.* **14** 99–106
[2] Levoy M 2006 Light fields and computational imaging *Comput. J.* **39** 46–55
[3] Georgiev T and Lumsdaine A 2010 Focused plenoptic camera and rendering *J. Electron. Imaging* **19** 021106
[4] Wu G, Masia B, Jarabo A, Zhang Y, Wang L, Dai Q, Chai T and Liu Y 2017 Light field image processing: an overview *IEEE J. Sel. Top. Signal Process.* **11** 1–29
[5] Ng R, Levoy M, Bredif M, Duval G, Horowitz M and Hanrahan P 2005 Light field photography with a hand-held plenoptic camera *Stanford Technical Report* CTSR pp 1–11
[6] Ihrke I, Restrepo J and Mignard-Debise L 2016 Principles of light field imaging: briefly revisiting 25 years of research *IEEE Signal Process. Mag.* **33** 59–69
[7] Wang T-C, Efros A A and Ramamoorthi R 2015 Occlusion-aware depth estimation using light-field cameras *IEEE Int. Conf. Computer Vision* pp 3487–95 (https://www.cv-foundation.org/openaccess/content_iccv_2015/html/Wang_Occlusion-Aware_Depth_Estimation_ICCV_2015_paper.html)
[8] Labios L 2017 4D camera could improve robot vision, virtual reality and self-driving cars *UC San Diego News Center* (https://ucsdnews.ucsd.edu/pressrelease/4d_camera_could_improve_robot_vision_virtual_reality_and_self_driving_cars)
[9] Dansereau D, Schuster G, Ford J and Wetzstein G 2017 A wide-field-of-view monocentric light field camera *Proc. CVPR IEEE* pp 5048–57 (http://openaccess.thecvf.com/content_cvpr_2017/html/Dansereau_A_Wide-Field-Of-View_Monocentric_CVPR_2017_paper.html)
[10] Lynch K 2011 Development of a 3D fluid velocimetry technique based on light field imaging *MSc Thesis* Auburn University
[11] Fahringer T W, Lynch K P and Thurow B S 2015 Volumetric particle image velocimetry with a single plenoptic camera *Meas. Sci. Technol.* **26** 1–25
[12] Fahringer T W and Thurow B S 2018 Plenoptic particle image velocimetry with multiple plenoptic cameras *Meas. Sci. Technol.* **29** 1–20
[13] Klemkowsky J N, Fahringer T W, Clifford C J, Bathel B F and Thurow B S 2017 Plenoptic background oriented Schlieren imaging *Meas. Sci. Technol.* **28** 1–18
[14] Sun J, Hossain M M, Xu C and Zhang B 2018 Investigation of flame radiation sampling and temperature measurement through light field cameras *Int. J. Heat Mass Transfer* **121** 1281–96
[15] Huang X, Qi H, Zhang X-L, Ren Y-T, Ruan L-M and Tan H-P 2018 Application of Landweber method for three-dimensional temperature field reconstruction based on the light-field imaging technique *J. Heat Transfer* **140** 082701
[16] Tan Z P and Thurow B S 2019 Time-resolved 3D flow-measurement with a single plenoptic camera *AIAA SciTech Forum and Exposition* (https://doi.org/10.2514/6.2019-0267)
[17] Tan Z P, Johnson K, Clifford C and Thurow B S 2019 Development of a modular, high-speed plenoptic-camera for 3D flow-measurement *Opt. Express* **27** 13400–15
[18] Drazic V, Sacre J-J, Schubert A, Bertrand J and Blonde E 2012 Optimal design and critical analysis of a high-resolution video plenoptic demonstrator *J. Electron. Imaging* **21** 1–10
[19] Levoy M, Ng R, Adams A, Footer M and Horowitz M 2006 Light field microscopy *Comput. Graph.* **25** 924–34
[20] Levoy M, Zhang Z and McDowall I 2009 Recording and controlling the 4D light field in a microscope using microlens arrays *J. Microsc.* **235** 144–62
[21] Liu Y, Hossain M M, Sun J, Xu C, Zhang B and Wang S 2017 Design a cage-typed light field camera system for flame measurement *IEEE Sens. J.*
[22] Fischer A, Kupsch C, Gurtler J and Czarske J 2015 High-speed light field camera and frequency division multiplexing for fast multi-plane velocimetry measurements *Opt. Express* **23** 24910–22
[23] Hall E M, Fahringer T W, Guildenbecher D R and Thurow B S 2018 Volumetric calibration of a plenoptic camera *Appl. Opt.* **57** 914–23

[24] Fahringer T W and Thurow B S 2013 The effect of grid resolution on the accuracy of tomographic reconstruction using a plenoptic camera *51st AIAA Aerospace Sciences Meeting including the New Horizons Forum and Aerospace Exposition*
[25] Fahringer T W and Thurow B S 2018 The effect of microlens size on the performance of single-camera plenoptic PIV *19th Int. Symp. on the Application of Laser and Imaging Techniques to Fluid Mechanics*
[26] Novara M and Scarano F 2012 Performance of motion tracking enhanced tomo-PIV on turbulent shear flows *Exp. Fluids* **52** 1027–41
[27] Lynch K P and Scarano F 2014 Experimental determination of tomographic PIV accuracy by a 12-camera system *Meas. Sci. Technol.* **25** 084003
[28] Elsinga G E, Scarano F, Wieneke B and van Oudheusden B W 2006 Tomographic particle image velocimetry *Exp. Fluids* **41** 933–47
[29] La Foy R R and Vlachos P 2013 Multi-camera plenoptic particle image velocimetry *10th Int. Symp. on Particle Image Velocimetry* (http://resolver.tudelft.nl/uuid:40f0a56c-9506-46c7-8022-e0f0c754aaa7)
[30] Lucy L B 1974 An iterative technique for the rectification of observed distributions *Astron. J.* **79** 745–54
[31] Richardson W H 1972 Bayesian-based iterative method of image restoration *J. Opt. Soc. Am.* **62** 55–9
[32] MATLAB Deblur image using Lucy–Richardson method *Mathworks* (www.mathworks.com/help/images/ref/deconvlucy.html)